International Journal of Hydrogen Energy 207 (2026) 153382

Contents lists available at ScienceDirect

International Journal of Hydrogen Energy

journal homepage: www.elsevier.com/locate/he

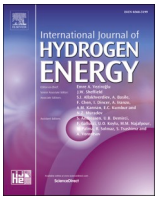

Investigation of methanol catalyst stability in presence of potential green hydrogen impurities

Lucas Warmuth [a,*], Clemens Hofsäß [a], Thomas A. Zevaco [a], Dieter Schild [b], Stephan Pitter [a], Jörg Sauer [a]

[a] Institute of Catalysis Research and Technology (IKFT), Karlsruhe Institute of Technology (KIT), 76344, Eggenstein-Leopoldshafen, Germany
[b] Institute for Nuclear Waste Disposal (INE), KIT, 76344, Eggenstein-Leopoldshafen, Germany

ARTICLE INFO

Keywords:
Green methanol
Hydrogen
Gas feed impurity
Catalyst deactivation
Sintering

ABSTRACT

Methanol synthesis' carbon footprint can be reduced using SynGas feeds from renewable power, but such feeds may strain catalysts due to impurities inherited from its production. Renewable sources include (biogas) pyrolysis, reforming, electrolysis, and shift reactions, whose possible poisons critically affect catalysis for future methanol production. In this work, $Cu/ZnO/ZrO_2$ and $Cu/ZnO/ZrO_2/SiO_2$ catalysts were tested under simulated feed conditions containing impurities from hydrogen sources. Since methane impurities and trace oxygen are rarely studied yet highly relevant, solar-powered methane or biogas pyrolysis and alkaline electrolysis were considered as case studies for a wide-rainging, sustainable hydrogen supply. Catalysts were investigated across their lifetime: before and after initial reduction, and during varying times on stream. Results show Cu^0 sintering strongly depends on the feed, whereas oxygen-containing feeds promote ZnO crystallization, reducing long-term performance. Incorporating silicon suppresses these effects, enabling more stable catalysts and supporting future use of solar-powered hydrogen feeds.

1. Introduction

Reaching a more sustainable production of platform chemicals implies a growing utilization of renewable sources necessary for the transition of the chemical industry [1]. For instance, CO_2 gained from point sources (e.g. coal power plants, cement plants, steel mills) or biogas-based sources delivering SynGas (e.g. gasification, pyrolysis, steam reforming) as well as hydrogen generated *via* solar-powered technologies (e.g. electrolysis, co-electrolyis with CO_2 or together with water-gas shift reaction) can be fed into methanol (MeOH) production plants [2], hence reducing their carbon footprint. Typical industrial $Cu/ZnO/Al_2O_3$-based (CZA) catalysts mainly employed in methanol synthesis nowadays [3] exhibit limited performance with CO_2-rich synthesis gas (SynGas) feeds. In particular, ZrO_2-promoted (CZZ) materials have been reported to combine comparable activity with higher stability at high CO_2/CO feed ratios, nicely coping with higher amounts of co-generated water [4].

Working with renewable, versatile sources implies a profound understanding of the role of potential H_2 impurities on the course of methanol synthesis and catalyst lifetime. In the case Cu/Zn-based (CZ) catalyst materials, poisons such as sulfur and halide as well as Ni and Fe compounds have been reported to reduce both catalyst stability and - over the catalyst lifetime - the integral productivity significantly [5]. To ensure a long-time stability including sufficient performance, these impurities are generally removed by so-called guard beds or using other technologies 2d,6. In comparison, degradation of the performance *via* coking or oxidation (e.g. by O_2 traces in the feed) are considered to be less likely due to the chosen process parameters [5,7]. However, their impact could be important in future scenarios of methanol production. An overview of possible deactivating pathways at typical methanol synthesis conditions is given in Table 1.

During the course of studies focusing on the deactivation mechanisms in the catalyst material, we could show recently that it is necessary to examine the material at critical points of the catalyst's lifetime (e.g. before reduction, after reduction, …) to gain an overview of the evolution of the catalysts' structure, morphology and porosity and also as a reference for the spent catalyst. Thereby, it was found that the main deactivation pathway for CZZ is sintering, which is accordance with literature about CZA 7a,f. In addition, it could be proven that re-oxidation of a spent CZZ catalyst (935 h Time on stream, ToS, further

* Corresponding author.
E-mail address: lucas.warmuth3@kit.edu (L. Warmuth).

https://doi.org/10.1016/j.ijhydene.2026.153382
Received 8 September 2025; Received in revised form 3 December 2025; Accepted 17 December 2025
Available online 12 January 2026

Table 1
Possible deactivation processes for CZ-based catalysts, their likelihood and prevention of those.

Deactivating process	Probability	Counteraction	Ref.
Coking	Very low	T < 300 °C/Introduce basic oxides into catalyst bed	5,6c, 7c,d
Poisoning	Low, if guard beds used	Guard beds	2d,5, 7c,d
Sintering	High	Lowering temperature/Water removal	7a,b,8
Oxidation	Low, if scrubbing	Scrubbing/Using more reductive feeds	2d,6e, 7c–g

Table 2
Studied application cases for hydrogen supply in methanol synthesis and their respective impurities as well as the possible deactivation mechanism.

Application Case[a]	Methane Pyrolysis	Alkaline Water Electrolysis
Main Impurity (Reason)	Methane (Unconverted)	Oxygen (Membrane Crossover)
Impurity Concentration	0-60 vol%	0–0.06 vol%
Possible Deactivation Mechanism[b]	Coking	Oxidation/Reduction Shuttle [11]
Literature	Duran et al. [12]	Bacquart et al. [13] Ursua et al. [14]

[a] Possibly coupled with MeOH synthesis.
[b] Refer to chapter "Results and Discussion".

details see Warmuth et al.) [7b] in air and a subsequent reduction step partly redisperse the Cu species, whereas ZnO coordination remains unaffected [7b].

Based on this, the hypothesis of this work is that the CZZ catalyst is likely to undergo different deactivation pathways if exposed to two exemplary hydrogen feeds (e.g. methane pyrolysis, equation (1) [9] and alkaline water electrolysis, equation (2) [10].

1	Methane pyrolysis [9]	$CH_4 \rightarrow C + 2H_2$	$\Delta H^0 = 37.7$ kJ mol^{-1}
2	Alkaline water electrolysis [10]	$2H_2O \rightarrow O_2 + 2H_2$	$\Delta H^0 = 237.1$ kJ mol^{-1}

These two different cases were considered to reflect possible scenarios for hydrogen supply from solar-based sources, supported by literature data regarding related feeds with their respective impurities and their concentrations. These impurities were admixed to SynGas components (e. g. $H_2/CO/CO_2$, 2.125/1/1) and fed into the methanol synthesis reactor (Table 2, details in the experimental section).

In order to compare with a benchmark, a system using pure SynGas feeds, a recent study on deactivation phenomena on CZZ is considered [7b]. Catalyst materials used in this work were Cu/ZnO/ZrO_2- (CZZ) and Cu/ZnO/ZrO_2/SiO_2-based (CZZSi) systems, evaluating the stability of the silicon-doped system in operation [15].

2. Results and discussion

2.1. First case: methane pyrolysis by concentrated solar power

In this case study, methane is co-fed with SynGas components for approx. 400 h ToS (denominated CZZ_{CH4}; 6.8 vol% CH_4, details in experimental section). The expected influence of the impurity would be coking, which could eventually block pores and channels of the methanol catalyst, even though the chosen reaction temperature is not preferring buildup of coke [16]. Above a certain detection limit, carbon and hydrogen contents of the carbonaceous deposits in the spent catalyst materials can be determined using CHNS analysis (Table 3). As a comparison, two samples of the same catalyst batch are activated similarly (e.g. reduced), one of these being only exposed to SynGas without methane (denominated CZZ_{SynGas}) while the second one is kept under argon at the respective methanol synthesis temperature (260 °C, denominated CZZ_{Ar}) and not exposed to neither methane nor feed gas. Measurements included the detection of coking (Fourier-transformed infrared spectroscopy, FTIR), evalutation of porosity changes (N_2 physisorption) and sintering (X-ray absorption spectroscopy, XAS). Generally, no significant changes in overall composition and especially carbon content could be observed. Nevertheless, considering the accuracy of the elemental analysis method, the error bar of carbon content analysis remains around 1 wt% [17], a small but relevant amount of carbon residues (e.g. < 1 wt%) in the catalyst cannot be ruled out. For this reason, surface analytics have to be considered as complementary analytical methods (e.g. FTIR, and N_2 physisorption).

Table 3
CHNS analyses for catalysts exposed to different feeds, investigated after different ToS. Reprinted original data for CZZ_{SynGas} with permission from Warmuth et al. Copyright 2024 American Chemical Society.

Denomination	ToS (h)	C (wt%)	H (wt%)	N (wt%)	S (wt%)
CZZ before catalysis	0	0.7	0.3	<0.1	not found
CZZ_{Ar}	50	not found	1.0	not found	not found
CZZ_{Ar}	455	not found	1.0	<0.1	not found
CZZ_{SynGas} [7b]	50	0.7	0.4	<0.1	<0.1
CZZ_{CH4}	50	not found	1.0	<0.1	not found
CZZ_{CH4}	455	not found	1.0	0.1	not found

FTIR did not show any significant carbon species' absorption bands (*SI:* Fig. S1), strongly suggesting the absence of coking products. In addition, the difference of specific surface area measured in N_2 physisorption (Fig. 1, compare *SI:* Fig. S2) is neglectable comparing the catalysts CZZ_{CH4} or CZZ_{Ar} to the reference data (CZZ_{SynGas}, Warmuth et al. [7b]/CZA_{SynGas}, Lunkenbein et al. [7a]) and indicates that no coke formation takes place in the material's pores. Interestingly, some changes in the surface area can be noticed comparing the catalysts investigated here. A sharp drop of the surface upon reduction (depicted as −50 h–0 h ToS) is observable followed by a minor decrease in the following ToS period, which is a typical pattern reported in literature for CZZ materials. CZZ_{Ar} also shows this behavior after 455 h ToS, suggesting that the main on-going deactivation process is a pure temperature-induced deactivation. It is conceivable that thermal treatment alone is responsible for the shrinking of the three-dimensional network, even without chemical side reactions able to degrade or clog

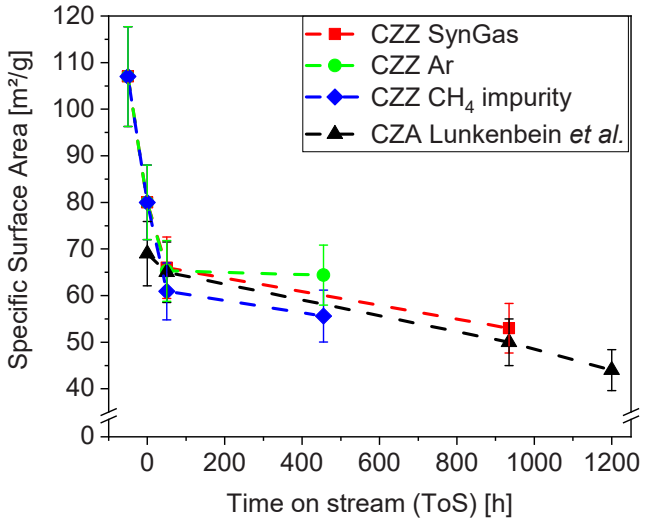

Fig. 1. Evolution of specific surface area of catalyst materials deactivated in different atmospheres. Calcined catalysts are denoted as −50 h ToS for visibility. Red: SynGas ($H_2/CO/CO_2$ = 2.125:1:1), Green: Argon, Blue: SynGas with CH_4 impurity, Black: CZA with typical SynGas as a reference. Lines are guide to the eye only. Reprinted original data for CZA with permission from Lunkenbein et al. Copyright 2015 John Wiley & Sons.

the catalytic material (e.g. as shown for CZZ_{Ar}). In more detail, sintering is a process mainly driven by heat and thus, it is also occurring in neutral gas feeds such as argon. This is an explanation of typical activity decrease observed for such catalyst systems, as reactant diffusion becomes more limited, regardless of the gas feed.

To complement the morphologic information, relative particle size changes could be observed by XAS analysis by comparing the signal height of the respective scattering path (= coordination sphere). In contrast to the results from physisorption and the conclusion thereof both, CZZ_{Ar} as well as CZZ_{CH4} show a small or even no significant increase in Cu–Cu scattering with increasing operation period. This fact suggests a low sintering rate of Cu species, quantitatively described in the Cu–Cu coordination number (CN; Fig. 2a). The coordination for Cu–Cu in CZZ_{SynGas} is higher in comparison, indicating stronger sintering for this feed composition. For ZnO, however, a similar sintering rate for all studied feeds (argon, SynGas, SynGas + CH_4 impurity) is assumed, as XAS analysis is showing similar trends of CN for all three tested catalyst materials (Fig. 2b).

Introducing CH_4 as purposeful feed impurity does not contribute to accelerated coking, contradicting the initial hypothesis. However, the relative influence of the temperature could be shown to be crucial for loss of porosity in all considered catalyst materials. In contrast, on the nanoscale, sintering of the Cu species is affected significantly by the respective gas feeds introduced (argon, SynGas, SynGas + CH_4 impurity), with SynGas showing the strongest enhancing effect.

2.2. Second case: alkaline water electrolysis using renewable power

In this scenario, oxygen present in the system *via* a hypothetical membrane crossover, is supposed to be the main impurity. It is delivered with the main SynGas feed over approx. 400 h ToS (approx. 0.06 vol% O_2 in H_2, catalysts denominated as CZZ_{O2}/$CZZSi_{O2}$) 2b,13,14. For assessing material changes, X-ray photoelectron spectroscopy (XPS, oxidation state), X-ray diffraction & XAS (XRD, crystallization & sintering) as well as chemisorption (active surface area & oxidation) are considered.

Under operating conditions, the partial pressure of oxygen varies depending on the gas feed. The total oxidation capability of the feed depends logically on the share of reductive species (e.g. H_2, CO). As indicator of this overall reductive potential, the partial pressure fraction p_{O2}/p_{H2+CO}, similar for all applied feeds in this work (Table 4) has to be used. According to literature, trace impurities of oxygen lead to enhanced sintering or segregation of a CZ-based catalyst by a redox shuttle between oxidized and reduced species (namely Cu^0/Zn^0 vs. CuO/ZnO) 7b,11,18. Thus, a more pronounced sintering mechanism can be logically expected for the catalyst materials (CZZ_{O2}/$CZZSi_{O2}$) compared to CZZ_{SynGas}.

Table 4
Comparison of the fraction of partial pressures (e.g O_2 in relation to H_2 or H_2 + CO, respectively) at typical operation/reduction conditions (SynGas/H_2 in N_2).

Gas mixture	p_{O2} [mbar]*	p_{O2}/p_{H2}	p_{O2}/p_{H2+CO}
SynGas	29	$2.8*10^{-3}$	$2.3*10^{-3}$
SynGas + O_2	640	$6.27*10^{-2}$	$5.08*10^{-2}$
5 vol% H_2/N_2	1	$5.8*10^{-3}$	$5.8*10^{-3}$
Ambient Air	212	4180	3483

**Assuming typical H_2/CO background concentrations in ambient air [19].
* Accounting for impurities given by the supplier (see experimental section).

As oxidation and subsequent increased sintering are the most likely pathways of deactivation 7a,b, XAS alongside XPS and XRD were employed. Throughout the catalyst's operation at the chosen operating conditions with oxygen-containing feed, no overall change in metal oxidation state could be detected evaluating the recorded XRD, XAS and XPS measurements (SI: Figs. S4–7). At first glance, this may seem surprising as the catalyst material is prone to oxidation due to the presence of nanosized particles of the reduced metals, e.g. Cu^0 and partly reduced ZnO (formation of Cu/Zn brass regions) 7b,20. The composition of the gas feed and its reductive capability strengthens the hypothesis of a redox shuttle, which can influence the particle growth and hence the catalyst's performance. In addition, the presence of oxygen traces alongside hydrogen will generate water ($K_p \approx 4*10^{42}$ at 260 °C) in the gas phase, thus enhancing an incidental hydrothermal sintering.

Using *Rietveld* refinement for the analysis of XRD measurements, Cu and ZnO crystallite sizes for CZZ_{SynGas} are observed to increase throughout the deactivation process up to 935 h ToS (Fig. 3a and b, green). In particular, results indicate sintering of Cu crystallites in CZZ_{O2} (red) as well as in $CZZSi_{O2}$ (cyan), being however less pronounced than in the case of CZZ_{SynGas}. In comparison, the exposure to oxygen traces affects the crystallization of ZnO much stronger in the case of the pure CZZ derivatives (CZZ_{O2}) than in the case of the silicon-doped CZZ material ($CZZSi_{O2}$), where the ZnO crystallite size remains similar over the whole deactivation period. In Fig. 3c and d, the increase of the relative crystallite sizes for Cu- and Zn-species is shown, the differences between CZZ_{SynGas} CZZ_{O2} and $CZZSi_{O2}$ being clearly visible.

A redispersion mechanism is already reported in literature for Cu [7b], in which air exposure after 1st reduction and a subsequent 2nd reduction reduces coordination number, indicating a particle size decrease. According to equation (3) and the literature, Cu oxidation is a two-step process, which is exothermic and reversible [21]. However, particle size is affected by exothermic reduction, as hotspot formation leads to sintering. Precisely, exact mechanisms of Cu oxidation with regard to particle morphology are complex and depend on many parameters.

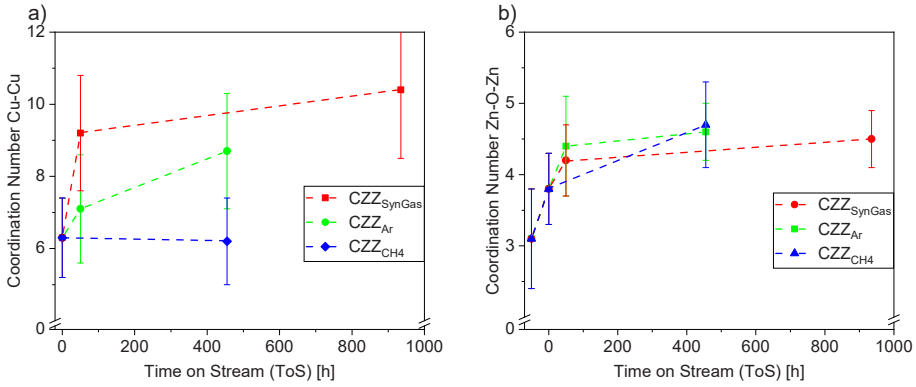

Fig. 2. (a) Cu and (b) Zn K edge-derived coordination numbers (Cu–Cu/Zn–*O*–Zn) of catalyst materials deactivated in different atmospheres over reaction time. Red: Typical SynGas, Green: Argon, Blue: SynGas with CH_4 impurity. Lines are guide to the eye only.

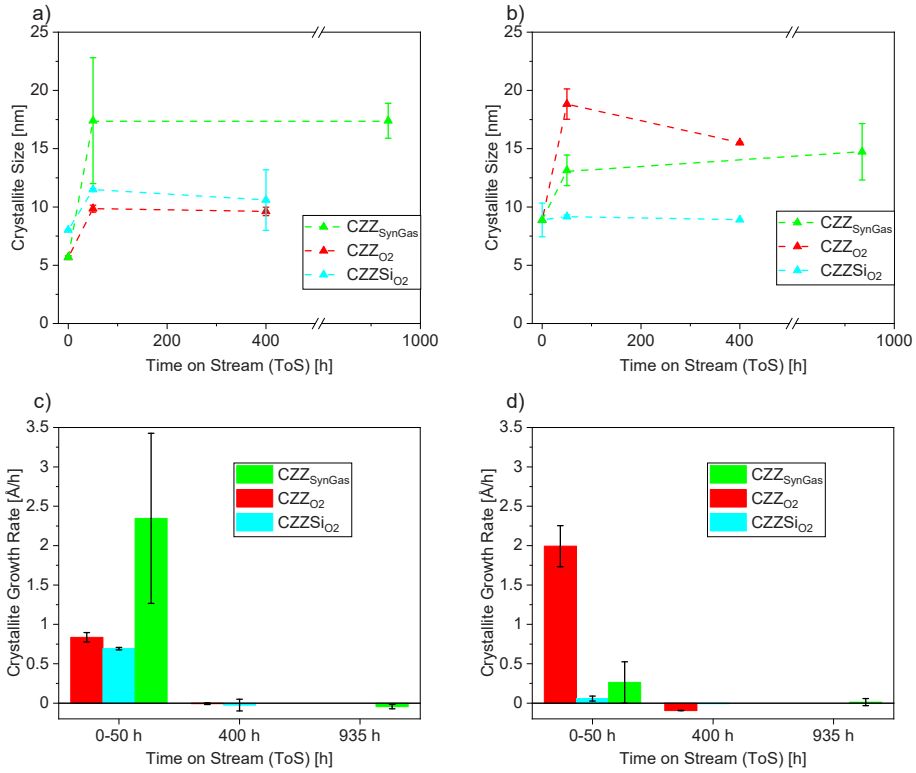

Fig. 3. Evolution of crystallite sizes obtained from *Rietveld* analysis of XRD different catalyst materials over ToS. a) Cu crystallite size, b) ZnO crystallite size, c) & d) Relative changes of the crystallite sizes within the first 50 h ToS and the rest of the deactivation period for c) Cu crystallite size d) ZnO crystallite size. Lines are a guide to the eye only.

3	Copper oxidation	$2\,Cu \underset{}{\overset{+\,1/2\,O_2}{\rightleftharpoons}} Cu_2O \overset{+\,1/2\,O_2}{\rightleftharpoons} 2\,CuO$	$\Delta H_1^0 = -169$ kJ mol^{-1} $\Delta H_2^0 = -12$ kJ mol^{-1}

In the mentioned literature mechanism of redispersion, for example, air contact is used to oxidize Cu. Therein p_{O2}/p_{H2} in air has been significantly higher than in this work (e.g. 4180 vs. 6.27*10^{-2}, respectively; Table 4), leading to different expected oxidation mechanisms.

As the crystallite growth of Cu is repressed in trace oxygen in this work, the first assumption would be that this probably takes place *via* the mentioned redispersion pathway. Another more likely explanation is however the decrease of the mean reduced fraction of Cu in the material. This would, in parallel, decrease its mean mobility and thus its sintering behavior. In contrast, ZnO has been reported to exhibit oxygen vacancies under reducing conditions [22]. This material phase, better described as ZnO_{1-x} (with $x \leq 1$), is expected to rapidly re-oxidize in the presence of O_2 impurities. Apparently, the interactions between the catalyst material and the feed gas clearly influence the catalyst material mainly by increasing the crystallization rate of ZnO (e.g. *via* alternating filling and inducing of oxygen vacancies).

Still, a similar crystallization of ZnO seems not to happen for CZZSi$_{O2}$. A possible explication for the stability of this material towards O_2 is also connected to the water management on the catalyst surface, with its formation being connected to an excess of H_2 and CO_2 in the feed gas. Water is known to accelerate hydrothermal sintering phenomena. In addition, the doping of CZZ material with silicon leads to the formation of a Si-stabilized phase. According to the literature dealing with CZA catalysts, this may lead to traces of a Zn_2SiO_4 phase or Si species being incorporated into the ZnO lattice (ZnO:Si) [15,23].

Coordination numbers, based on EXAFS analysis is employed to support these initial findings regarding particularly the particle size increase. Therein, only slight sintering of Cu/Zn species is proven, indicated by a rising coordination number, CN (*SI:* Fig. S5). For both Cu and Zn K-edge, this increase in CN is similar for all species (e. g. CZZ$_{SynGas}$, CZZ$_{O2}$, CZZSi$_{O2}$). Overall, the tendencies of particle growth on the nanoscale (≠ crystallization rate) determined by XAS are irrespective of oxygen exposure or catalyst material in the respective cases.

In order to evaluate the nature of the catalyst's surface more precisely, chemisorption analytics were employed (e.g. H_2-based temperature-programmed reduction; TPR, N_2O titration). A standard analytic procedure usually reported for CZ catalysts consists in assessing first reducibility and course of the reduction of the catalysts *via* TPR (**4**) and then in evaluating the active surface of the catalyst *via* N_2O chemisorption (**5**). The evaluation of the minimal N_2O amount necessary to oxidize the surface of the active catalyst particles is performed *via* pulse chemisorption.

4	H_2-TPR	$CuO/ZnO/ZrO_2 \rightarrow Cu/ZnO_{1-x}/ZrO_2 + H_2O$
5	N_2O titration	$Cu/ZnO_{1-x}/ZrO_2 + (1+x)\,N_2O \rightarrow Cu_2O/ZnO/ZrO_2 + (1+x)\,N_2$

In the initial TPR, CZZ and CZZSi are both reducible, as expected for metal oxide mixtures generated *via* calcination at 350 °C (Fig. 4). For the reduced and spent catalysts stored under argon, no significant H_2 uptake is observed, as one would anticipate. Mild reoxidation with N_2O pulses would expectedly only oxidize species with a high active surface and materials with finely dispersed morphology (e.g. Cu^0, ZnO_{1-x}), and would potentially show a decrease of the active Cu surface area upon

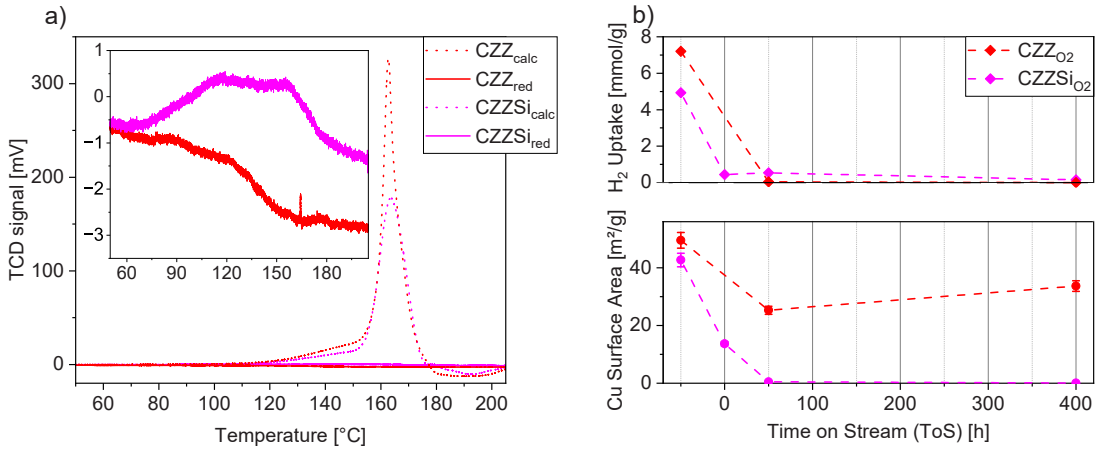

Fig. 4. (a) H_2-TPR profiles and (b) H_2 uptake calculated from H_2-TPR for CZZ_{O2} and $CZZSi_{O2}$ as well as Cu surface area from N_2O pulse chemisorption.

deactivation and/or sintering.

Interestingly, N_2O pulses did not reoxidize CZZSi species, as shown by the vey low measured dispersion and the resulting calculated Cu surface areas being nearly zero. Strong sintering phenomena happening more likely during the exothermic methanol synthesis contribute to lower the overall specific surface area (99 m^2/g reduced to 71 m^2/g after H_2-TPR) leaving less fine surface ready for mild oxidation. The sintered surface of the spent catalyst is then more comparable to a Cu "sheet" displaying ZnO regions. However another scenario cannot be completely ruled out: In accordance with studies dealing with other reducible species in inert matrices [24], the catalyst material might undergo the formation of an inert layer over the reactive surface of Cu^0 (and oxygen vacancies in ZnO, if any), thus preventing a subsequent oxidation *via* N_2O pulses.

To summarize, the reduced mean mobility of Cu^0 limits the negative sintering effects, caused by traces of O_2 in the feed. On the other hand, crystallization of ZnO is enhanced by those O_2 traces, revealing the sensitivity of ZnO_{1-x} species to their surrounding atmosphere. In fact, Si promotion, prevents crystallization of ZnO species, assumedly by forming a Zn_2SiO_4 or ZnO:Si species. Forming those seems to be a key in hydrothermal and oxygen exposure stability, as shown above.

3. Conclusion

The presence of impurities in SynGas composition, produced from renewable H_2 sources (e.g. CH_4 pyrolysis or H_2O electrolysis) can impact catalyst stability. In this work, the use of specific gas feeds in the methanol synthesis, ranging from pure argon to SynGas (CO_2/CO/H_2), with or without CH_4 or O_2 and the resulting structural changes were evaluated.

The comparison of catalysts exposed to typical conditions of the methanol synthesis, with or without argon as inert gas, reveals that sintering can merely happen *via* thermal stress, without intervention of reactive gases. Surprisingly, thermal stress alone reduces the pore volume significantly and to the same extent as SynGas operation does. This implies that transport limitations are reigned by temperature-induced pore size changes. Working with SynGas atmosphere increases the share of sintering in the catalyst samples, depending on the respective gas composition (e.g. argon, pure SynGas, SynGas + CH_4), whereas ZnO seems not to be directly influenced in its aggregation behaviour. In comparison, the nature of the gas phase influence directly the particle size within the Cu phase, confirming again the central role of Cu as active species in this catalysis. On the other hand, traces of methane have no influence on the morphology of the catalysts and do not lead to the formation of coke deposits with the described conditions as it has been suggested in the literature.

Oxygen as feed impurity contributes to counteract the sintering of Cu^0, probably *via* the decrease of the mean fraction of reduced Cu. Still, it supports the crystallization of the ZnO phase within the catalyst materials, which is the critical point for a long-term stability of the CZ(A) catalysts. A definite enrichment of CZZ with silicon (1 wt%) delivers materials with better long-time stability, probably due to the formation of "hydrothermal sintering resistant" Si-doped ZnO phases or/and of stable Zn_2SiO_4 regions within the CZZ materials as suggested in literature.

Based on these findings, the oxygen-sensitivity of different phases in the catalyst material will be addressed (e.g. ZnO_{1-x}, ZrO_{2-x}) in detail to understand activating and deactivating processes and consequently improve the CZZ catalyst materials to perform efficiently and stable in a wide range of feed impurities.

4. Experimental section

4.1. Continuous co-precipitation

The CZZ precursor materials are prepared by continuous co-precipitation with subsequent aging. The details are described elsewhere [25]. In short, a solution of 117.42 g of copper(II)nitrate trihydrate ($Cu(NO_3)_2{\cdot}3H_2O$, Merck, Darmstadt, Germany, 99.5 %) 72.29 g of zinc nitrate hexahydrate ($Zn(NO_3)_2{\cdot}6H_2O$, Alfa Aesar, Thermo Fischer, Kandel, Germany, 99 %) and the amount given in Table 5 of the respective promoting precursor (to yield CZZ/CZZSi) in 3 L of distilled water is mixed under high volume flow to a solution of 1.01 mol L^{-1} $NaHCO_3$ at 55 °C. The suspension is transferred directly to a double-jacketed 5000 mL glass vessel and aged at 55 °C until tipping point and 30 min beyond under stirring (1000 rpm). Following the aging period, the suspension is filtered and the solid residue is washed with distilled water. The solid is then dried and calcined in air at 350 °C with a heating ramp of 3 K/min for 4 h resulting in 30 g of CZZ metal oxide pre-catalyst with a composition of 64/31/5 (Cu/Zn/Zr; mol%; normalized). It is known that this standardized catalyst converts feeds rich in CO_2 and that performance is comparable to commercial ones in a wide range of conditions (30–60 barg, 180–260 °C, CO_2/CO_x = 0.04–1) 4b,8a,25a,26.

Table 5
Parameters of synthesis for CZA/CZZ/CZZSi and determined metal contents.

Precursor (in addition to Cu^{2+} and Zn^{2+})	Introduced Amount [g]	Aging Temperature [°C]	Cu [mol %]	Zn [mol %]	Si [mol %]	Zr [mol %]
$NaSiO_3$ solution (26 wt% SiO_2) + $ZrO(NO_3)_2{\cdot}6H_2O$	5.62 + 19.24	85	60	32	2	10
$ZrO(NO_3)_2{\cdot}6H_2O$	27.48	55	64	31	–	5

4.2. Catalyst deactivation and anoxic sampling

The plant **Par**allel **C**atalyst **A**ging **S**etup (PaCAS) is used for systematic catalyst deactivation and is described elsewhere [7b].

In short, initial reduction was performed at a pressure of 2.5 bar and 5 vol-% H_2 in 95 vol-% N_2. The temperature program for the reduction is chosen as follows: 90 °C for 20 min and heating with ramp of 10 K/min at 220 °C, then holding this temperature for 60 min. After cooling the reactors down to ambient temperature under anoxic atmosphere (Argon). The catalyst ageing is performed with a gas feed containing 17 vol-% H_2, 4 vol-% CO, 4 vol-% CO_2 and 75 vol-% N_2 and cofeeding the respective impurity (see Table 6).

The inlet pressure and the pressure retention valve are set to 70 bar and 60 bar, respectively. After heating to 260 °C, the gas inlet is changed to the synthesis gas feed. To achieve a high dwell time, the catalyst mass-based volume flow is set to 5.00 L_N/g^*h to evenly age the catalyst. The flow rate ($\dot{V}_{2reactors}$) for both reactors is calculated as given in equation (3):

$$\dot{V}_{2r} = \frac{2\vartheta_{GHSV}\, m_{catalyst}}{60000} \quad (3)$$

After reaction, the reactors are cooled to ambient temperature at an argon flow rate of 100 mL_N/min and the catalysts bed are transferred into a glovebox (*MBraun)* by maintaining the materials in the reactor blocks under argon atmosphere (99.9999 % pure Argon is used). All gases were used as received without additional drying of purification (99.999 % N_2, 99.999 % H_2, 99.995 % CO_2, 99.97 % CO).

4.3. X-ray absorption spectroscopic experiments

The X-ray absorption spectroscopic (XAS) measurements were performed were performed at the beamline BM23 at the European Synchrotron Radiation Facility with a spectroscopic reaction cell reported in literature. on chamber I_0 was filled with 1.570 bar N_2 and ion chamber I_1 and I_2 with 0.333 bar Ar, all complemented up to 2 bar with He. The samples were measured in transmission mode at the Cu and Zn K edges, placed between I_0 and I_1. Between I_1 and I_2, reference foils (Cu and Zn) [27] were placed and measured simultaneously with the catalyst samples for energy scale alignment purposes.

The used beam size was 1.7 mm (horizontal) x 0.6 mm (vertical). Both K edges were recorded in one scan from 8.8 keV to 10.4 keV using the Cu foil for alignment. For the measurements, 5 mg of the catalyst and 25 mg of dried hexagonal BN are mixed in the glovebox and filled into glass capillaries (*Hilgenberg*). Afterwards, the capillaries are molten to keep the samples under argon atmosphere to prevent oxidation.

For analysis of the XANES and EXAFS data Athena and Artemis-IFEFFIT/Demeter package (version 0.9.26) [28] is used. The data are calibrated using tabulated values for metallic reference foils ($E_{Cu,K}$ = 8979 eV; $E_{Zn,K}$ = 9659 eV). Afterwards, the cubic spline background is subtracted to eliminate the non-structural portion of absorption data and the spectra are normalized [29]. For the refinement, a k-range of 3.0 $Å^{-1}$ to 9.5 $Å^{-1}$ for the Cu K-edge and 3.0 to 6.5 $Å^{-1}$ for Zn K-edge is used. The amplitude factors for (S_0^2) for Cu and for Zn are set to 0.926 and 0.626, respectively (determined from the fitting of the experimental data on references; additional parameters in *SI:* Table S1 & Table S2), and the coordination numbers for Cu in the first shell as well as the Zn–*O*–Zn shell were also evaluated.

Table 6
Dosed impurities and their respective concentrations.

Denomination	Impurity Source	Dosed to Concentration [vol%]	Absolute Error Sum [±vol%]
CZZ_{O2}	1 vol% O_2 in N_2	$1*10^{-2}$ (17 vol% H_2 * 0.06 vol% O_2 within)	$1*10^{-3}$
CZZ_{CH4}	40 vol% CH_4 in N_2	6.8 (17 vol% H_2 * 40 vol% CH_4 within)	$8*10^{-2}$

4.4. X-ray photoelectron spectroscopy (XPS)

For XPS analysis, the system *PHI 5000 VersaProbe II (ULVAC-PHI Inc.*) with a monochromatic Al K_α, $h\nu = 1486.7$ eV, scanning microprobe X-ray source is used. Subsequent, the X-ray source power and the X-ray spot size diameter are adjusted to 30 W and 170 μm, respectively. By providing a pass energy of 187.85 eV of the analyser, survey scans are recorded. Areas of the elemental lines were determined after Shirley background subtraction within an error of ±10–20 %. Considering elemental sensitivity factors, asymmetry parameters and transmission function of the analyser, the relative atomic concentrations are calculated. Narrow scans of the elemental lines are recorded at 23.5 eV pass energy, which yields an energy resolution of 0.69 eV FWHM at the Ag $3d_{5/2}$ elemental line of pure silver. In addition, calibration of the binding energy scale of the spectrometer is achieved *via* using well-established binding energies of elemental lines of pure metals (monochromatic Al K_α: Cu $2p_{3/2}$ at 932.62 eV, Au $4f_{7/2}$ at 83.96 eV) [30]. The error of measured binding energies is estimated to be within ±0.2 eV.

For the XPS measurements 5 mg catalyst is deposited on an indium foil inside a glovebox. Then, the sample is put in a transfer vessel and moved into the XPS analysis chamber under anoxic atmosphere. The Fermi edges of the valence band prove that the samples are conductive and grounded. Furthermore, the measured binding energies of the elemental lines are compared to a reference database [31]. *ULVAC-PHI MultiPak* program, version 9.9 was used for the data analysis.

4.5. Combustion analysis for determination of light elements (CHNS)

CHNS analysis was used to investigate poisoning of a catalyst and is carried out by weighing the sample in tin boats and heating them (1100 °C) in the presence of O_2 producing the product gases CO_2, H_2O, NO_2, and SO_2 [32]. This is followed by controlled reduction of NO_2 to N_2 by passing the gas over Cu at 850 °C [32b]. Finally, the product gas is captured by a column and identified using a thermal conductivity detector [32a]. Here, a complete setup called *vario EL cube* from *Elementar* is used.

4.6. Inductive coupled plasma - optical emission spectroscopy (ICP-OES)

For the ICP-OES analysis of the CZZ catalyst, a hydrofluoric acid digestion of 20 mg sample is carried out, enabling the determination of Cu, Zn, Zr and poisons such as Fe or Ni (e.g. originating from the metal tubing). Digestion is performed with an *Anton Paar Multiwave 3000* microwave oven using HF (40 %) in Teflon™ vessels at 240 °C for 2h. Subsequent dilution is in 0.2 M HNO_3 Suprapur. For analysis, an *Agilent 725 ICP-OES* spectrometer with argon as plasma gas at 15 L/min and plasma stimulation at 40 MHz, 2 kW, is applied.

4.7. X-ray diffraction (XRD)

X-ray diffractograms were measured using a Panalytical X'Pert Pro X-ray diffractometer (Malvern Panalytical GmbH, Kassel, Germany) with Bragg-Brentano geometry and Cu K_α radiation with a Ni filter. In order to prevent oxidation of the samples, a special holder with PEEK cap has been used (Malvern Panalytical). The diffractograms are recorded in the range 5–80° over a period of 120 min. The reflections are evaluated using the QualX software (version 2.24) [33] and compared to references from the Crystallography Open Database (COD) [34]. To obtain the composition and particle size of the samples analyzed by XRD, *Rietveld* refinement is performed using the open-source program Profex 5.0.2 from N. Döbelin [35].

4.8. N_2-physisorption

N_2 physisorption measurements [36] were carried out on Quantachrome NOVA 2000e and NOVA 3200e devices (Anton Paar GmbH, Graz, Austria) at 77 K to determine pore size and active catalyst surface area. Samples (250 mg, grain size 250–500 µm) were degassed for 12 h at 230 °C. Isotherms are evaluated with the Brunnauer–Emmett–Teller (BET) model [37] in the range of 0.05–0.1 p/p_0 The pore size distributions are calculated according to the Barret–Joyner–Halenda (BJH) method [38] using the desorption branch of the isotherm.

4.9. Chemisorption

For N_2O chemisorption measurements, an Altamira AMI-300 equipped with a Thermal Conductivity Detector was used for the combined TPR - N_2O Pulse Chemisorption analytic. The AMI 300 equipment is equipped with four Mass Flow Controllers responsible for the relevant four inlets groups, allowing thus a greater flexibility regarding the gas mixtures: Carrier (4 lines), Treatment (4 lines), Blend (2 lines) and Aux (iliary) (2 lines). The chemisorption equipment was operated *via* the proprietary control software ("AMI 300") from the Altamira software package, using dedicated experiment programs (.exp) whereas the evaluation of the TPR and N_2O-pulse chemisorption profiles was performed using the "AMI-Analysis" part of the software package. TPR and N_2O profiles in this publication have been generated using the OriginPro 2022 software package (version 9.9.0.225). The pretreatment of the samples and the experimental procedure were carried out using a specially developed method, which is partly based on a literature-known method for N_2O pulse flow experiments [39]. Ca. 100 mg of catalyst were placed in a U-shaped quartz reactor and first dried under argon at 120 °C (flow 30 ml/min, temperature ramp 10 °C/min, holding 30 min at 200 °C) followed by cooling down to 50 °C under Ar flow (20 °C/min). The temperature was raised afterwards from 50 °C to 250 °C at a rate of 1 °C/min (250 °C holding for 45min) in a gas mixture containing 5 vol% H_2/Ar (10 vol% H_2/Ar, flow 15 ml/min diluted with pure Ar @ 15 ml/min). The TCD was calibrated before the experiment using the same diluted 5 % H_2/Ar gas mixture (flow 30 ml/min, 5 pulses, volume of the loop 518 ml). After reduction, with the sample kept under Argon flow all the time, a rough determination of the active surface of the Cu-containing catalysts can be performed *via* N_2O pulse chemisorption. The principle of the titration relies on a controlled oxidation of the surface of the sample with this mild oxidant, sending pulses of a defined volume (518 ml of 5 vol% N_2O in He) and quantifying the liberated N_2 *via* evaluation of the recorded TCD profiles against a calibration gas mixture (5 vol% N_2/Helium). The pulse chemisorption is actually performed using a gas mixture of 5 vol% N_2O in Helium (using a 10 vol% N_2O/He - @ 15 ml/min – diluted with pure helium @ 15 ml/min).

CRediT authorship contribution statement

Lucas Warmuth: Writing – original draft, Visualization, Validation, Supervision, Project administration, Methodology, Investigation, Formal analysis, Data curation, Conceptualization. **Clemens Hofsäß:** Writing – review & editing, Visualization, Validation, Methodology, Investigation, Formal analysis. **Thomas A. Zevaco:** Writing – review & editing, Validation, Methodology, Investigation, Formal analysis, Data curation. **Dieter Schild:** Writing – review & editing, Validation, Resources, Methodology, Investigation, Formal analysis, Data curation. **Stephan Pitter:** Writing – review & editing, Supervision, Project administration, Funding acquisition, Formal analysis, Conceptualization. **Jörg Sauer:** Writing – review & editing, Supervision, Resources, Project administration, Funding acquisition, Conceptualization.

Funding sources

The authors are grateful to the Helmholtz Innovation Pool "Solar Hydrogen", a project within the Helmholtz Program *Materials and Technologies for the Energy Transition* (MTET), project no. 38.04.03.

Declaration of competing interest

The authors declare that they have no known competing financial interests or personal relationships that could have appeared to influence the work reported in this paper.

Acknowledgment

We would like to thank Mariam Schulte, Lorena Baumgarten for performing *ex situ* measurements at the European Synchrotron Radiation Facility (ESRF). Additionally, we are thankful for their help and technical support during experiments by Diana Deutsch, Ricki Drexler, Siegbert Johnsen and Dorian Weiler (IKFT). Moreover, we are grateful to the whole IKFT analytics and the people providing them, especially, Thomas Otto and Armin Lautenbach.

Appendix A. Supplementary data

Supplementary data to this article can be found online at https://doi.org/10.1016/j.ijhydene.2026.153382.

ABBREVIATIONS

BET	Brunnauer–Emmett–Teller
BJH	Barret–Joyner–Halenda
CN	Coordination number
CZ	Cu/ZnO
CZA	Cu/ZnO/Al2O3
CZZ	Cu/ZnO/ZrO2
CZZSi	Cu/ZnO/ZrO2/SiO2
EDXS	energy-dispersive X-ray spectroscopy
EXAFS	extended X-ray absorption fine structure
FTIR	Fourier-transform infrared
GHSV	gas hourly space velocity
HAADF STEM	high-angle annular dark-field scanning transmission electron microscopy
MeOH	Methanol
ICP OES	Inductive coupled plasma - optical emission spectroscopy
LCA	Linear combination analysis
PaCAS	Parallel Catalyst Aging Setup
ToS	Time on stream
H2 TPR	H2 based temperature-programmed reduction
SEM	scanning electron microscopy
SMSI	strong metal support interaction
TPR	temperature programmed reduction
XANES	X-ray absorption near edge structure
XAS	X ray absorption spectroscopy
XRD	X ray diffraction
XPS	X ray photoelectron spectroscopy

References

[1] Lee H, Calvin K, Dasgupta D, Krinner G, Mukherji A, Thorne PW, Trisos C, Romero J, Aldunce P, Barrett K, Blanco G, Cheung WWL, Connors S, Denton F, Diongue-Niang A, Dodman D, Garschagen M, Geden O, Hayward B, Jones C, Jotzo F, Krug T, Lasco R, Lee Y-Y, Masson-Delmotte V, Meinshausen M, Mintenbeck K, Mokssit A, Otto FEL, Pathak M, Pirani A, Poloczanska E, Pörtner H-O, Revi A, Roberts DC, Roy J, Ruane AC, Skea J, Shukla PR, Slade R, Slangen A, Sokona Y, Sörensson AA, Tignor M, van Vuuren D, Wei Y-M, Winkler H, Zhai P, Zommers Z, Hourcade J-C, Johnson FX, Pachauri S, Simpson NP, Singh C, Thomas A, Totin E, Arias P, Bustamante M, Elgizouli I, Flato G, Howden M, Méndez-Vallejo C, Pereira JJ, Pichs-Madruga R, Rose SK, Saheb Y, Sánchez Rodríguez R, Ürge-Vorsatz D, Xiao C, Yassaa N, Alegría A, Armour K, Bednar-Friedl B, Blok K, Cissé G, Dentener F, Eriksen S, Fischer E, Garner G, Guivarch C, Haasnoot M, Hansen G, Hauser M, Hawkins E, Hermans T, Kopp R, Leprince-Ringuet N, Lewis J, Ley D, Ludden C, Niamir L, Nicholls Z, Some S, Szopa S,

Trewin B, van der Wijst K-I, Winter G, Witting M, Birt A, Ha M, Kim J, Haites EF, Jung Y, Stavins R, Orendain DJA, Ignon L, Park S, Park Y, Reisinger A, Cammaramo D, Fischlin A, Fuglestvedt JS, Matthews JR, Péan C. In: Sixth assessment report of the intergovernmental Panel on climate change. Geneva: Intergovernmental Panel on Climate Change (IPCC); 2023.

[2] a) Niquini GR, Münzer P, Ebrahim-Moghaddam M, Warmuth L, Herrera Delgado K, Pitter S, Dahmen N, Sauer J. Chem Ing Tech 2024;96:100–13. https://doi.org/10.1002/cite.202300221.b) Ivanova M, Peters R, Müller M, Haas S, Seidler MF, Mutschke G, Eckert K, Röse P, Calnan S, Bagacki R, Schlatmann R, Grosselindemann C, Schäfer L-A, Menzler NH, Weber A, de Krol R van, Liang F, Abdi FF, Brendelberger S, Neumann N, Grobbel J, Roeb M, Sattler C, Duran I, Dietrich B, Hofberger C, Stoppel L, Uhlenbruck N, Wetzel T, Rauner D, Hecimovic A, Fantz U, Kulyk N, Harting J, Guillon O. Angew Chem 2023. https://doi.org/10.1002/anie.202218850.c) Flores-Granobles M, Saeys M. Energy Environ Sci 2020;13:1923–32. https://doi.org/10.1039/d0ee00787k.d) Schittkowski J, Ruland H, Laudenschleger D, Girod K, Kähler K, Kaluza S, Muhler M, Schlögl R. Chem Ing Tech 2018;90:1419–29. https://doi.org/10.1002/cite.201800017.

[3] a) Fujita S-i, Satriyo AM, Shen GC, Takezawa N. Catal Lett 1995;34:85–92. https://doi.org/10.1007/bf00808325.b) Bems B, Schur M, Dassenoy A, Junkes H, Herein D, Schlögl R. Chemistry (Weinheim an der Bergstrasse, Germany) 2003;9:2039–52. https://doi.org/10.1002/chem.200204122.c) Behrens M, Girgsdies F, Trunschke A, Schlögl R. Eur J Inorg Chem 2009;2009:1347–57. https://doi.org/10.1002/ejic.200801216.d) Behrens M. J Catal 2009;267:24–9. https://doi.org/10.1016/j.jcat.2009.07.009.e) Behrens M, Brennecke D, Girgsdies F, Kißner S, Trunschke A, Nasrudin N, Zakaria S, Idris NF, Hamid SBA, Kniep B, Fischer R, Busser W, Muhler M, Schlögl R. Appl Catal Gen 2011;392:93–102. https://doi.org/10.1016/j.apcata.2010.10.031.f) Behrens M, Kasatkin I, Kühl S, Weinberg G. Chem Mater 2010;22:386–97. https://doi.org/10.1021/cm9029165.

[4] a) Wild S, Lacerda de Oliveira Campos B, Zevaco TA, Guse D, Kind M, Pitter S, Herrera Delgado K, Sauer J. Reaction Chemistry & Engineering. 2022. https://doi.org/10.1039/d1re00470k.b) Wild S, Polierer S, Zevaco TA, Guse D, Kind M, Pitter S, Herrera Delgado K, Sauer J. RSC Adv 2021;11:2556–64. https://doi.org/10.1039/d0ra09754c.c) Tada S, Katagiri A, Kiyota K, Honma T, Kamei H, Nariyuki A, Uchida S, Satokawa S. J Phys Chem C 2018;122:5430–42. https://doi.org/10.1021/acs.jpcc.7b11284.d) Arena F, Italiano G, Barbera K, Bordiga S, Bonura G, Spadaro L, Frusteri F. Appl Catal Gen 2008;350:16–23. https://doi.org/10.1016/j.apcata.2008.07.028.e) Larmier K, Liao W-C, Tada S, Lam E, Verel R, Bansode A, Urakawa A, Comas-Vives A, Copéret C. Angew Chem Int Ed 2017;56:2318–23. https://doi.org/10.1002/anie.201610166.f) Beck A, Newton MA, de Water L G A van, Bokhoven J A van. Chem Rev 2024;124:4543–678. https://doi.org/10.1021/acs.chemrev.3c00148.

[5] Kung HH. Catal Today 1992;11:443–53. https://doi.org/10.1016/0920-5861(92)80037-n.

[6] a) Hegen O, Salazar Gómez JI, Grünwald C, Rettke A, Sojka M, Klucken C, Pickenbrock J, Filipp J, Schlögl R, Ruland H. Chem Ing Tech 2022;94:1405–12. https://doi.org/10.1002/cite.202200015.b) Schittkowski J, Zeidler-Fandrich B, Müller T, Schlögl R, Ruland H. Chem Ing Tech 2022. https://doi.org/10.1002/cite.202200019.c) He J, Laudenschleger D, Schittkowski J, Machoke A, Song H, Muhler M, Schlögl R, Ruland H. Chem Ing Tech 2020;92:1525–32. https://doi.org/10.1002/cite.202000045.d) Girod K, Lohmann H, Schlüter S, Kaluza S. Processes 2020;8. https://doi.org/10.3390/pr8121673.e) Nitsche T, Budt M, Apfel UP. Chem Ing Tech 2020;92:1559–66. https://doi.org/10.1002/cite.202000052.

[7] a) Lunkenbein T, Girgsdies F, Kandemir T, Thomas N, Behrens M, Schlögl R, Frei E. Angew Chem Int Ed 2016;55:12708–12. https://doi.org/10.1002/anie.201603368.b) Warmuth L, Steurer M, Schild D, Zimina A, Grunwaldt J-D, Pitter S. ACS Appl Mater Interfaces 2024;16:8813–21. https://doi.org/10.1021/acsami.3c17383.c) Roberts GW, Brown DM, Hsiung TH, Lewnard JJ. Ind Eng Chem Res 1993;32:1610–21. https://doi.org/10.1021/ie00020a012.d) Twigg MV. Top Catal 2003;22:191–203. https://doi.org/10.1023/a:1023567718303.e) Liang B, Ma J, Su X, Yang C, Duan H, Zhou H, Deng S, Li L, Huang Y. Ind Eng Chem Res 2019;58:9030–7. https://doi.org/10.1021/acs.iecr.9b01546.f) Fichtl MB, Schlereth D, Jacobsen N, Kasatkin I, Schumann J, Behrens M, Schlögl R, Hinrichsen O. Appl Catal Gen 2015;502:262–70. https://doi.org/10.1016/j.apcata.2015.06.014.g) Fichtl MB, Schumann J, Kasatkin I, Jacobsen N, Behrens M, Schlögl R, Muhler M, Hinrichsen O. Angew Chem Int Ed 2014;53:7043–7. https://doi.org/10.1002/anie.201400575.

[8] a) Schulte ML, Truttmann V, Doronkin DE, Baumgarten L, Nicolai A, Beltran DAM, Summ FJ, Kiener C, Warmuth L, Pitter S, Saraci E, Grunwaldt JD. Angew Chem Int Ed Engl 2025:e202423281. https://doi.org/10.1002/anie.202423281.b) Lacerda de Oliveira Campos B, John K, Beeskow P, Herrera Delgado K, Pitter S, Dahmen N, Sauer J. Processes 2022;10:1535. https://doi.org/10.3390/pr10081535.

[9] Sánchez-Bastardo N, Schlögl R, Ruland H. Ind Eng Chem Res 2021;60:11855–81. https://doi.org/10.1021/acs.iecr.1c01679.

[10] Tuysuz H. Acc Chem Res 2024;57:558–67. https://doi.org/10.1021/acs.accounts.3c00709.

[11] Clariant international Ltd., muttenz. 2017.

[12] Durán I, Dietrich B, Hofberger C, Stoppel L, Uhlenbruck N, Wetzel T, Coronado JM. Int J Energy Res 2023;2023:1–23. https://doi.org/10.1155/2023/3684046.

[13] Bacquart T, Murugan A, Carré M, Gozlan B, Auprêtre F, Haloua F, Aarhaug TA. Int J Hydrogen Energy 2018;43:11872–83. https://doi.org/10.1016/j.ijhydene.2018.03.084.

[14] Ursúa A, San Martín I, Barrios EL, Sanchis P. Int J Hydrogen Energy 2013;38:14952–67. https://doi.org/10.1016/j.ijhydene.2013.09.085.

[15] Barrow N, Bradley J, Corrie B, Cui Y, Tran TD, Erden TE, Fish A, Garcia M, Glen P, Mistry N, Nicholson M, Roloff-Standring S, Sheldon D, Smith T, Summer A, Din KU, Macleod N. Sci Adv 2024;10. https://doi.org/10.1126/sciadv.adk2081. eadk2081.

[16] Bertau M, Schmidt F, Wernicke H-J, Offermanns H, Plass L. Methanol: the basic chemical and energy feedstock of the future: asinger's vision today. Berlin: Springer; 2014.

[17] Kuveke REH, Barwise L, van Ingen Y, Vashisth K, Roberts N, Chitnis SS, Dutton JL, Martin CD, Melen RL. ACS Cent Sci 2022;8:855–63. https://doi.org/10.1021/acscentsci.2c00325.

[18] a) Andreasen JW, Rasmussen FB, Helveg S, Molenbroek A, Ståhl K, Nielsen MM, Feidenhans'l R. J Appl Crystallogr 2006;39:209–21. https://doi.org/10.1107/s0021889806003098.b) Chaturvedi S, Rodriguez J, Hrbek J. Surf Sci 1997;384:260–75. https://doi.org/10.1016/s0039-6028(97)00232-x.c) Maroie S, Haemers G, Verbist JJ. Appl Surf Sci 1984;17:463–7. https://doi.org/10.1016/0378-5963(84)90006-0.

[19] a) Westra IM, Scheeren HA, Stroo FT, van Heuven S, Kers BAM, Peters W, Meijer HAJ. Sci Rep 2024;14:24147. https://doi.org/10.1038/s41598-024-76373-2.b) Ward K, Hansen K, Cassidy E, Doermann L, Przyborski P, Dauphin L, Liang W, Garrison M, Levy R. NASA Earth Observatory, Washington. 2023.

[20] Pandit L, Boubnov A, Behrendt G, Mockenhaupt B, Chowdhury C, Jelic J, Hansen AL, Saraçi E, Ras EJ, Behrens M, Studt F, Grunwaldt JD. ChemCatChem 2021;13:4120–32. https://doi.org/10.1002/cctc.202100692.

[21] Aromaa J, Kekkonen M, Mousapour M, Jokilaakso A, Lundström M. Corros Mater Degrad 2021;2:625–40. https://doi.org/10.3390/cmd2040033.

[22] Mockenhaupt B, Gieser J, Najafishirtari S, Baumgarten L, Jelic J, Lunkenbein T, Ras E-J, Grunwaldt J-D, Studt F, Behrens M. J Catal 2024;439. https://doi.org/10.1016/j.jcat.2024.115785.

[23] a) Dalebout R, Barberis L, Totarella G, Turner SJ, La Fontaine C, de Groot FMF, Carrier X, van der Eerden AMJ, Meirer F, de Jongh PE. ACS Catal 2022;12:6628–39. https://doi.org/10.1021/acscatal.1c05101.b) Iwasaki K, Ashida Y, Matsumura D, Kawakami K, Shibuya K, Tazawa M, Tsuji T, Shimizu H. J CO2 Util 2025;97. https://doi.org/10.1016/j.jcou.2025.103111.

[24] a) Vandenberg M, Polarz S, Tkachenko O, Klementiev K, Bandyopadhyay M, Khodeir L, Gies H, Muhler M, Grunert W. J Catal 2006;241:446–55. https://doi.org/10.1016/j.jcat.2006.05.020.b) Ou Y, Zhang T, Lv L, Tang W, Tang S. Colloids Surf A Physicochem Eng Asp 2023;676. https://doi.org/10.1016/j.colsurfa.2023.132167.

[25] a) Guse D, Warmuth L, Herfet M, Adolf K, Zevaco TA, Pitter S, Kind M. Catalysts 2024;14. https://doi.org/10.3390/catal14080517.b) Guse D, Polierer S, Wild S, Pitter S, Kind M. Chem Ing Tech 2022;94:314–27. https://doi.org/10.1002/cite.202100197.

[26] a) Rodrigues Niquini G, Herrera Delgado K, Pitter S, Sauer J. Reaction Chemistry & Engineering. 2026. https://doi.org/10.1039/d5re00330j.b) Lacerda de Oliveira Campos B, Herrera Delgado K, Pitter S, Sauer J. Ind Eng Chem Res 2021;60:15074–86. https://doi.org/10.1021/acs.iecr.1c02952.

[27] Pandit L, Serrer MA, Saraçi E, Boubnov A, Grunwaldt JD. Chemistry–Methods 2022;2. https://doi.org/10.1002/cmtd.202100078.

[28] Ravel B, Newville M. J Synchrotron Radiat 2005;12:537–41. https://doi.org/10.1107/s0909049505012719.

[29] Newville M, Livins P, Yacoby Y, Rehr JJ, Stern EA. Phys Rev B 1993;47:14126–31. https://doi.org/10.1103/PhysRevB.47.14126.

[30] Seah MP, Gilmore IS, Beamson G. Surf Interface Anal 1998;26:642–9. https://doi.org/10.1002/(sici)1096-9918(199808)26:9<642::Aid-sia408>3.0.Co;2-3.

[31] a) Moulder J, Stickle W, Sobol P, Bomben KD. Handbook of X-Ray Photoelectron Spectroscopy. Physical Electronics, Inc.; 1995.b) Powell C. X-ray Photoelectron Spectroscopy Database XPS. Version 4.1, NIST Standard Reference Database 20. 1989.

[32] a)P. E. Hemming, Exeter Analytical (UK) Ltd. b) Braun EI, Pantano P. Carbon 2014;77:912–9. https://doi.org/10.1016/j.carbon.2014.06.005.

[33] Altomare A, Corriero N, Cuocci C, Falcicchio A, Moliterni A, Rizzi R. J Appl Crystallogr 2015;48:598–603. https://doi.org/10.1107/s1600576715002319.

[34] a) Vaitkus A, Merkys A, Grazulis S. J Appl Crystallogr 2021;54:661–72. https://doi.org/10.1107/S1600576720016532.b) Vaitkus A, Merkys A, Sander T, Quiros M, Thiessen PA, Bolton EE, Grazulis S. J Cheminform 2023;15:123. https://doi.org/10.1186/s13321-023-00780-2.

[35] Doebelin N, Kleeberg R. J Appl Crystallogr 2015;48:1573–80. https://doi.org/10.1107/s1600576715014685.

[36] Thommes M, Kaneko K, Neimark AV, Olivier JP, Rodriguez-Reinoso F, Rouquerol J, Sing KSW. Pure Appl Chem 2015;87:1051–69. https://doi.org/10.1515/pac-2014-1117.

[37] Brunauer S, Emmett PH, Teller E. J Am Chem Soc 1938;60:309–19. https://doi.org/10.1021/ja01269a023.

[38] Barrett EP, Joyner LG, Halenda PP. J Am Chem Soc 1951;73:373–80. https://doi.org/10.1021/ja01145a126.

[39] Hinrichsen O, Genger T, Muhler M. Chem Eng Technol 2000;23:956–9. https://doi.org/10.1002/1521-4125(200011)23:11<956::Aid-ceat956>3.0.Co;2-l.